Surfaces and Interfaces 89 (2026) 109116

Contents lists available at ScienceDirect

Surfaces and Interfaces

journal homepage: www.sciencedirect.com/journal/surfaces-and-interfaces

Pump-probe microscopy reveals the mechanisms of double-pulse processing of metals

Maximilian Spellauge [a], David Redka [a], Stefan Remund [b], Beat Neuenschwander [b], Heinz P. Huber [a], Daniel.J. Förster [a,*]

[a] Laser Center HM, Munich University of Applied Sciences HM, Lothstraße 34, 80335 Munich, Germany
[b] Institute for Applied Laser, Photonics and Surface Technologies ALPS, Bern University of Applied Sciences, Pestalozzistraße 20, 3400 Burgdorf, Switzerland

ARTICLE INFO

Keywords:
Double-pulse processing
Burst processing
Time-resolved microscopy
Redeposition
Ablation rate

ABSTRACT

Recent advances in ultrafast laser technology have enabled the delivery of high pulse energies at MHz repetition rates, but often at peak fluences well above the optimal range for efficient ablation. Temporal pulse shaping can mitigate this issue by distributing energy across multiple sub-pulses separated by defined inter-pulse delays. However, when delays are too short, interaction of preceding pulses with the ablation plume severely reduces ablation efficiency. This study investigates the physical origins of such efficiency losses in double-pulse ablation of copper and steel. Ablation depth and efficiency were measured for inter-pulse delays between 12.2 ns and 231.8 ns. These results were compared with time-resolved pump–probe microscopy measurements of the transient reflectance to quantify plume shielding. A strong correlation is found between second-pulse efficiency and plume transmittance. Plume shielding is identified as the dominant mechanism limiting ablation efficiency in both materials. For copper, redeposition further reduces efficiency, leading to strongly reduced net ablation at inter-pulse delays shorter than 50 ns. Maximum losses of up to 63% in Cu and 21% in steel are observed at inter-pulse delays of 12.2 ns. Full recovery of second-pulse efficiency is achieved at inter-pulse delays exceeding 150 ns for Cu and 30 ns for steel, corresponding to maximum feasible repetition rates of 6.7 MHz and 33 MHz, respectively. These findings highlight the importance of optimizing inter-pulse delay in double-pulse laser processing and establish time resolved microscopy as a powerful tool for predicting inter-pulse delay dependent ablation efficiency in double-pulse laser processing.

1. Introduction

Ultrashort pulse laser processing, employing pulse durations from a few hundred femtoseconds to several picoseconds, is a versatile technique for high-precision manufacturing applications such as drilling, cutting, and milling [1]. These short pulse durations enable precise [2,3] and efficient [4] material processing due to negligible thermal diffusion [5] and the build-up of high tensile stresses that result in photomechanical material removal [6], respectively.

Besides the pulse duration [7,8], the peak fluence [9] also significantly influences the ablation efficiency, defined as the removed volume per incident pulse energy. This quantity is also commonly referred to as the specific removal rate [10] or the energy-specific ablation volume [11]. Ablation efficiency models and experimental studies [9,12] show that the highest ablation efficiency is achieved when processing with a peak fluence of $\Phi_0 = e^2 \bullet \Phi_{thr}$, where Φ_{thr} denotes the ablation threshold fluence of the material.

As laser technology has advanced significantly over the past decade, state-of-the-art laser systems now commonly deliver pulse energies of up to several hundred microjoules at repetition rates of several megahertz [13]. With beam waist diameters typically in the range of several tens of micrometers, this corresponds to available peak fluences exceeding 100 J/cm^2. Given that the single-pulse ablation threshold fluence of industrially relevant metals ranges from 0.2 J/cm^2 for steel to 2 J/cm^2 for Cu [7], the available peak fluence surpasses the optimum value of $e^2 \bullet \Phi_{thr}$ by one to two orders of magnitude. In multi-pulse processing, where the same position is repeatedly irradiated, this discrepancy is further amplified due to incubation effects, which can reduce the ablation threshold by up to an order of magnitude [14]. As a result, in the presence of incubation during multi-pulse processing, the available peak

* Corresponding author.
E-mail addresses: maximilian.spellauge@hm.edu (M. Spellauge), david_sebastian.redka@hm.edu (D. Redka), stefan.remund@bfh.ch (S. Remund), beat.neuenschwander@bfh.ch (B. Neuenschwander), heinz.huber@hm.edu (H.P. Huber), daniel.foerster@hm.edu (Daniel.J. Förster).

https://doi.org/10.1016/j.surfin.2026.109116
Received 14 October 2025; Received in revised form 5 February 2026; Accepted 25 March 2026
Available online 26 March 2026

fluence can exceed the optimal value by two to three orders of magnitude.

To avoid inefficient material processing at excessively high peak fluences, while still making full use of the high pulse energies available from state-of-the-art laser systems, two main pulse shaping strategies have been employed. First, spatial pulse shaping, in which the laser energy is divided among multiple beams, with each beam carrying the optimal peak fluence [15]. Second, temporal pulse shaping, where a single pulse is split into a burst of several sub-pulses, each carrying the optimal peak fluence, with inter-pulse delays ranging from several hundred picoseconds (GHz-burst) to several nanoseconds (MHz-burst) [11].

The first investigations of the physical mechanisms responsible for the strong dependence of ablation efficiency on the inter-pulse delay during burst material processing were carried out using double pulses [11,16–19]. For inter-pulse delays shorter than the material-specific mechanical relaxation time, which is on the order of a few picoseconds for stainless steel and approximately 20 ps for Cu [7], the ablation efficiency does not change significantly compared to single-pulse processing [16–20]. This reflects a regime in which the inter-pulse delay is short enough to maintain stress confinement [6,19,21].

When the inter-pulse delay is increased beyond the mechanical relaxation time to a few tens of picoseconds, a decrease in ablation efficiency is observed. This is attributed to the partial compensation of the tensile wave generated by the first pulse by the compressive wave generated by the second pulse [20,22]. A further increase of the inter-pulse delay into the range of a few hundred picoseconds, which corresponds to the GHz-burst regime, leads to an additional reduction in ablation efficiency due to shielding of the subsequent pulse by the ablation plume or even redeposition of material ablated by the first pulse [19,23,24]. Depending on the material, the ablation efficiency can decrease by 50% or more, and in some cases by up to 90%, at inter-pulse delays ranging from 100 ps to several nanoseconds [23].

If the inter-pulse delay is further increased, shielding of the subsequent pulse by the ablation plume is commonly considered the dominant factor limiting ablation efficiency, while redeposition becomes less significant with increasing delay [11]. A pronounced signature of plume shielding in ultrashort-pulse MHz-burst ablation is the frequently reported odd–even dependence of ablation efficiency, with odd sub-pulse numbers contributing significantly more to material removal than even sub-pulse numbers [25–28]. This odd–even behavior is commonly interpreted as a direct consequence of plume shielding: an odd pulse generates a dense ablation plume that partially absorbs or scatters the subsequent even pulse, which therefore ablates less and produces a thinner plume, allowing the next odd pulse to ablate efficiently again [28].

However, the identification of plume shielding described above is largely based on final-state ablation metrics such as ablation efficiency or crater morphology. Only a few works provide more direct experimental support for plume shielding by probing plume dynamics during ultrashort-pulse burst ablation [26,29]. In particular, in-situ imaging has been used to track the temporal evolution of the ablation plume during MHz-burst ablation, revealing the ablation plume to persist on nanosecond timescales and correlating qualitatively with the reduced ablation efficiency of subsequent pulses [26,29]. While these observations are consistent with plume-mediated attenuation, they do not provide a quantitative measure of laser energy loss within the plume. Beyond experimental studies, plume shielding has been addressed mainly in computational works, where laser–plume interaction is explicitly modeled [30,31]. These studies predict plume-induced optical shielding and a corresponding reduction in ablation efficiency at nanosecond-scale inter-pulse delays due to absorption and scattering of the laser pulse. While such simulations provide valuable physical insight into plume shielding mechanisms, they do not establish an experimental, time-resolved correlation between plume transmittance and final-state ablation efficiency under ultrashort-pulse MHz-burst processing conditions.

As a result, experimental, time-resolved characterization of plume-induced shielding as a function of inter-pulse delay in ultrashort-pulse MHz-burst ablation, and its quantitative correlation with final-state ablation efficiency under processing-relevant conditions, remains limited. Motivated by this, the present work aims to quantify how plume shielding reduces ablation efficiency as a function of inter-pulse delay under processing-relevant conditions in ultrashort-pulse MHz-burst laser processing.

To establish this link under processing-relevant conditions, double-pulse ablation efficiency is measured from scanning experiments, for inter-pulse delays in the range of several tens of nanoseconds corresponding to the MHz-burst regime. This regime is selected because plume shielding dominates, while material redeposition plays a minor role and interference of pressure waves is no longer present [11]. In parallel, time-resolved pump–probe microscopy is used to quantify the transient plume transmittance on comparable timescales. Cu and stainless steel were selected as contrasting materials due to their vastly different thermal and electronic properties. Stainless steel exhibits strong energy confinement due to its low thermal conductivity and fast electron–phonon coupling, while Cu exhibits weaker confinement because of its high thermal conductivity and slower electron–phonon coupling [7,19].

2. Materials and methods

2.1. Sample preparation and characterization

Copper and austenitic stainless steel (AISI304, hereafter referred to as steel) were used throughout this study.

For the scanning double-pulse processing experiments detailed in Section 2.2, standard Cu (C12200) and AISI304 sheets were used. Both materials had a thickness of 2 mm and were laser-cut into 50 mm x 50 mm specimens prior to double-pulse ablation. The samples were mechanically lapped to achieve a low surface roughness of a few tens of nanometers.

For the time-resolved experiments described in Section 2.3, Cu with a purity of 99.999% and the austenitic stainless steel AISI304 were purchased from *Goodfellow* GmbH. Both samples had a thickness of 1 mm and a diameter of 25 mm. Subsequent sanding and polishing of the samples was performed to achieve a smooth sample surface, which is required to accurately measure the transient reflectance with the employed PPM technique. Confocal microscopy measurements (*Leica*, Ergoplan) were performed to determine the root mean square surface roughness S_q, yielding $S_q = 16$ nm and $S_q = 2$ nm for Cu and steel, respectively.

2.2. Double-pulse processing

For double-pulse ablation, an ultrafast laser source (Lumentum Operations LLC, PicoBlade 2) was used, emitting linearly polarized TEM_{00} pulses at a wavelength of 1064 nm with a pulse duration of 10 ps and a repetition rate of 200 kHz, corresponding to a fixed temporal spacing of 5 μs between emission events. The beam quality was specified as $M^2 = 1.2$. In double-pulse mode each emission event consisted of two energetically equal pulses separated by a variable inter-pulse delay δ_t, adjustable in integer multiples of 12.2 ns. Equal energy for both pulses was ensured using a calibrated monitoring photodiode. To isolate the effect of the second pulse, a single-pulse ablation process was performed in which each emission event consisted of a single pulse with the same energy as one pulse from the double-pulse configuration.

Laser machining was performed in ambient air using a galvanometer scanner (Scanlab GmbH, ExcelliScan) equipped with a 160 mm focal length f-theta lens. Prior to entering the scanning optics, the beam diameter was adjusted using a telescope to achieve a beam waist radius of$w_0 = (16 \pm 1)$ μm, measured in the focal plane with a rotating slit

beam profiler (Thorlabs Inc.). Squares of 1 mm x 1 mm were machined on the sample surface. The scanning speed was chosen to achieve a lateral irradiation event spacing of $h = 8$ µm in both directions. Due to the resulting 75% beam overlap in both directions, each scan pass yields 16 pulses per position in the single-pulse configuration and 32 pulses per position in the double-pulse configuration. The scan pattern was repeated $N = 48$ times in the double-pulse configuration and $N = 96$ times in the single-pulse configuration, resulting in a total number of pulses per position of $N_{tot} = 1536$ in both cases. Since each pulse contained the same pulse energy E_P, this ensured that the total energy delivered to the target was identical in both the double-pulse and single-pulse configuration.

The ablated features reached depths of several tens of micrometers, allowing accurate determination of the total ablation depth d_{tot} using white-light interferometric microscopy (gbs, smartWLI prime). The ablation efficiency η_{abl}, defined as the ablated volume per incident pulse energy, was calculated by Eq. (1).

$$\eta_{abl} = \frac{d_{tot} \cdot h^2}{N \cdot E_P} \tag{1}$$

2.3. Pump-probe microscopy

An ultrafast laser source (*Spectra Physics*, FemtoREGEN) emitting linearly polarized TEM_{00} pulses with a wavelength of 1056 nm, a pulse duration of 500 fs, and a repetition rate of 500 Hz was used throughout the pump-probe microscopy (PPM) experiments. The pulses were split into pump and probe pulses with an energy ratio of 9:1 using a half-wave plate combined with a polarizing beam splitter and all experiments were conducted in ambient air.

The pump-pulses were guided through another half-wave plate polarizing beam splitter combination to allow a continuous adjustment of the pulse energy. Following this, a mechanical shutter selected a single pump pulse from the pulse train. This configuration ensured the delivery of a single, temporally isolated pulse to the sample, in contrast to the double-pulse emission events used in the ablation experiments described in Section 2.2. Subsequently, a pulse stretcher was used to increase the pulse duration to 10 ps (FWHM) to match the pulse duration employed in the corresponding double-pulse experiments. Finally, the p-polarized pump pulse was focused onto the sample surface under an incidence angle of 35° by means of a plano-convex lens with a focal length of 100 mm, resulting in an elliptical beam profile on the target surface. The resulting minor-axis beam waist radius of $w_0 = (15 \pm 0.5)$ µm and beam quality of $M^2 = 1.2$ were measured by a focal beam profiler (PRIMES GmbH, MicroSpotMonitor) and matched the parameters for the double pulse processing described in Section 2.2.

A second harmonic generation unit converted the wavelength of the probe-pulse to 528 nm. Following this, the probe pulse was temporally delayed with respect to the pump-pulse by means of an optical delay line. The resulting delay time Δt could be adjusted between −50 ps and +4 ns. Here Δt is used to denote the pump–probe delay time, distinguishing it from the inter-pulse delay δ_t used in the double-pulse experiments. For longer delay times, a second electronically delayed ps-laser (*InnoLas* GmbH, PicoloAOT) with a wavelength of 532 nm and a pulse duration of 500 ps was utilized, enabling delay times up to $\Delta t = 1$ s. The probe-pulse was then guided onto the sample surface through a quarter-wave plate and a microscope objective (50x, NA = 0.42), resulting in circularly polarized pulses that imaged the transient reflectance change at a selected delay time Δt onto a camera (*PCO* AG, pco.pixelfly usb). A tube lens situated in front of the camera imaged the sample surface onto the camera. Additionally, a band-pass filter centered at 520 nm with a bandwidth of 20 nm was installed in front of the camera in order to suppress undesired scattered light from the pump-pulse.

As the transient reflectance change was probed at peak fluences greater than the ablation threshold fluence, the exposed material was irreversibly damaged. Thus, for each desired delay time Δt, the sample was displaced by 100 µm to guarantee a pristine surface without previously induced laser damage. For each delay time Δt, two images were recorded. The first image (with corresponding reflectance R_0) was recorded 1 s before pump-pulse impact and the second image (with corresponding reflectance $R(\Delta t)$) at the desired delay time Δt. The transient relative reflectance change was then calculated by Eq. (2).

$$\frac{\Delta R}{R_0} = \frac{R(\Delta t) - R_0}{R_0} \tag{2}$$

Finally, the spatially resolved relative reflectance change was azimuthally averaged. A more detailed description of the PPM setup, including a schematic depiction and details of the image post-processing procedure, can be found elsewhere [32].

3. Results

As a starting point, Section 3.1 investigates the dependence of double-pulse ablation depth and ablation efficiency on the incident peak fluence and inter-pulse delay. Following this, the ablation efficiency is compared to single-pulse ablation dynamics recorded by PPM in Section 3.2.

3.1. Peak fluence dependent final state ablation characteristics

Double pulses consisting of two energetically equal pulses with variable inter-pulse delays ranging from 12.2 ns to 231.8 ns were employed to machine square patterns of 1 mm x 1 mm using the scanning parameters described in Section 2.2. All ablation depths and surface morphologies discussed in the following were evaluated in the central region of the scanned squares and are representative of the surface morphology within the processed area.

Under the assumption of an exponential decay of the laser fluence with depth, which is well justified for ultrashort-pulse laser–metal interaction [33], and the existence of an ablation threshold fluence Φ_{thr} that must be exceeded to initiate material removal, the dependence of the ablation depth per pulse d_{abl} on the incident peak fluence per pulse Φ_0 can be described by the following semi-empirical equation [9,12].

$$d_{abl} = d_{eff} \cdot \ln\left(\frac{\Phi_0}{\Phi_{thr}}\right) \tag{3}$$

Here, Φ_{thr} denotes the ablation threshold fluence, i.e. the incident fluence at which measurable material removal sets in. The parameter d_{eff} represents an effective energy penetration depth that incorporates optical absorption as well as ultrafast energy transport processes such as thermal diffusion during the pulse [34] and ballistic electron transport [35]. The ablation depth per pulse was obtained by dividing the total ablation depth d_{tot} by the total number of incident pulses per position N_{tot} Since the ablation threshold fluences reported here are obtained from depth measurements under repeated irradiation during the scanning experiments described in Section 2.2, they are henceforth referred to as the scanning ablation threshold fluence. This distinction is introduced to avoid confusion with the single-pulse ablation threshold fluence, which was independently determined using the PPM setup described in Section 2.3.

3.1.1. Copper

For Cu, Fig. 1a depicts the ablation depth as a function of the incident peak fluence for inter-pulse delays of 12.2 ns, 122.0 ns, and 231.8 ns. In the peak fluence range from approximately 0.7 J/cm^2 to 2.0 J/cm^2, the ablation depth follows the logarithmic behavior predicted by Eq. (3), corresponding to the spallation regime [36]. At higher peak fluences, deviations from this behavior become apparent as the ablation depth increases more rapidly, indicating the emergence of a second slope within the phase explosion regime [36]. The scanning ablation threshold

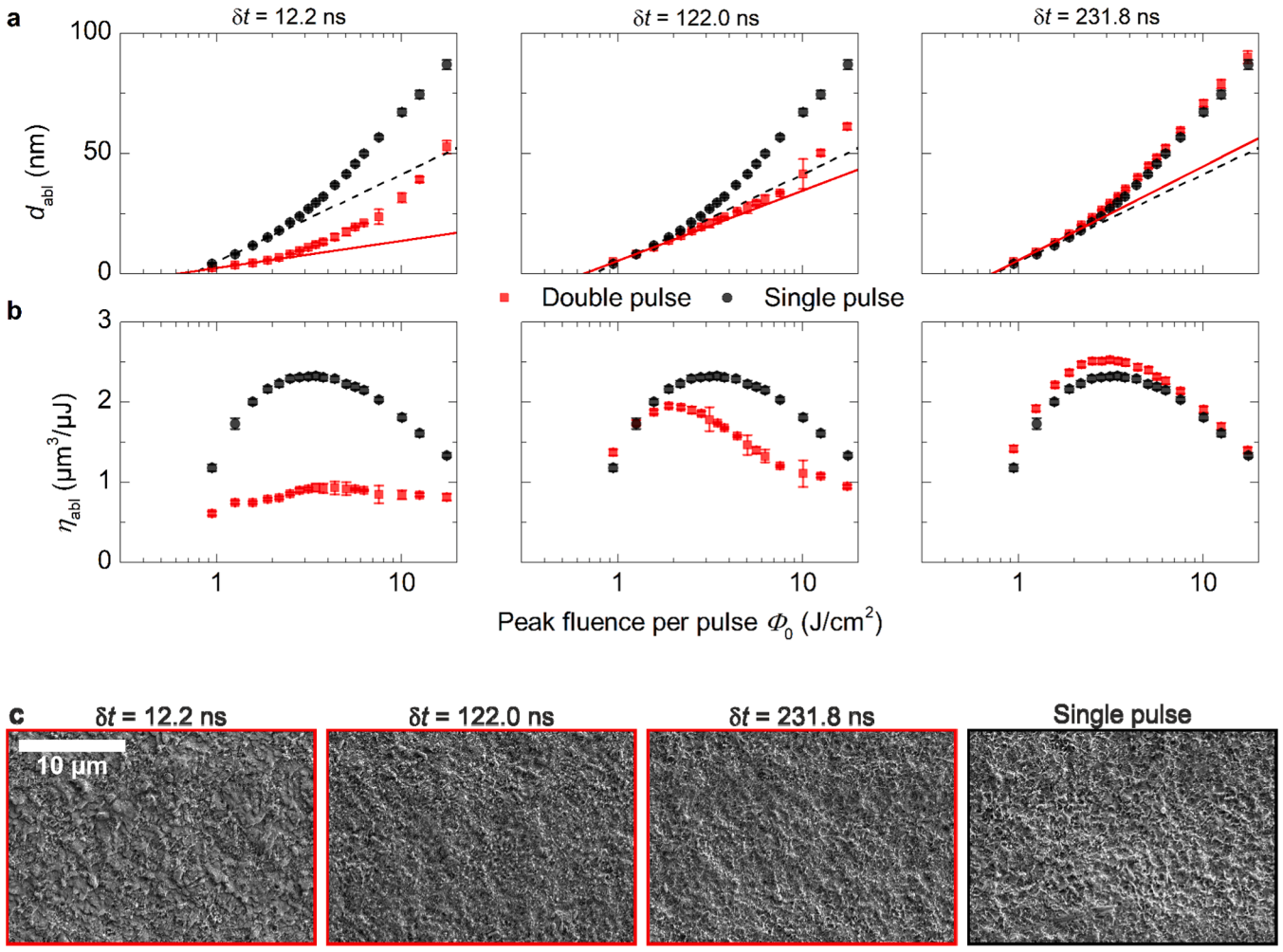

Fig. 1. Final-state ablation characteristics of Cu processed using the double-pulse and single-pulse configurations. In both cases, the laser emitted pulses with a duration of 10 ps (FWHM) and a central wavelength of 1064 nm. In the double-pulse configuration, each emission event consisted of two energetically equal pulses separated by an inter-pulse delay δ_t, whereas in the single-pulse configuration each emission event consisted of a single pulse. The emission events were spaced by 5 μs, and the total number of incident pulses per position was 1536 in both configurations. Inter-pulse delays of 12.2 ns (left column), 122.0 ns (middle column), and 231.8 ns (right column) are shown. a) Ablation depth per pulse d_{abl} as a function of incident peak fluence per pulse Φ_0. The scanning ablation threshold fluences Φ_{thr} were determined by fitting Eq. (3) to the data in the spallation regime for peak fluences $\Phi_0 < 2$ J/cm^2. For the double-pulse configuration the obtained fits are shown by solid red lines, whereas for the single-pulse case the fits are shown by dashed black lines. b) Ablation efficiency η_{abl} as a function of Φ_0. c) SEM images of the surface morphology after laser structuring at a fixed peak fluence of $\Phi_0 = 3.0 \bullet \Phi_{thr}$, corresponding approximately to the peak fluence at which the maximum ablation efficiency is reached in the single-pulse configuration. Images are shown for three different inter-pulse delays in the double-pulse configuration (12.2 ns, 122.0 ns, and 231.8 ns), as well as for the single-pulse configuration. The scale bar in the left image applies to all images. The ablation depths and surface morphologies were evaluated in the central region of the 1 mm x 1 mm scanned squares and are representative of the surface morphology within the processed area.

fluence and effective penetration depth were determined by fitting Eq. (3) within the spallation regime, i.e., for peak fluences up to 2.0 J/cm^2. The resulting values are summarized in Table 1.

A slight increase in the scanning ablation threshold fluence is observed with increasing inter-pulse delay, rising from 0.62 J/cm^2 at δ_t = 12.2 ns to 0.72 J/cm^2 at δ_t = 231.8 ns. The latter value approximately matches the single-pulse configuration scanning ablation threshold fluence of 0.73 J/cm^2 (see Table 1). In addition, the effective penetration depth within the spallation regime increases with inter-pulse delay, from d_{eff} = 5 nm at δ_t = 12.2 ns to d_{eff} = 17 nm at δ_t = 231.8 ns, with the latter being in good agreement with the single-pulse configuration value of 16 nm (see Table 1).

The ablation efficiency η_{abl}, calculated from the ablation depth using Eq. (1), is plotted as a function of the incident peak fluence for different inter-pulse delays in Fig. 1b. For the shortest inter-pulse delay of 12.2 ns, the ablation efficiency increases with peak fluence and then plateaus, showing no distinct local maximum. In contrast, for longer inter-pulse delays of 122.0 ns and 231.8 ns, a clear maximum emerges at peak fluences approximately three to four times the scanning ablation threshold fluence. For these delays, the fluence-dependent trend consists of an initial increase, a peak, and a subsequent decrease in efficiency, closely resembling the behavior observed for the single-pulse configuration. The corresponding maximum ablation efficiency values for each inter-pulse delay are summarized in Table 1. Notably, the maximum ablation efficiency exhibits a strong dependence on the inter-pulse delay: it increases from 0.93 μm^3/μJ at δ_t = 12.2 ns to 2.52 μm^3/μJ at δ_t = 231.8 ns, representing a relative increase of approximately 60 %. At the longest delay, the ablation efficiency exceeds the value of 2.32 μm^3/μJ measured for the single-pulse configuration by approximately 9%.

The corresponding SEM images of the laser-processed surfaces at a fixed peak fluence of $\Phi_0 = 3.0 \bullet \Phi_{thr}$ are shown in Fig. 1c. This peak fluence was chosen as the maximum ablation efficiency is reached here (see Fig. 1b). All surfaces exhibit microstructures with irregular features and no clear periodicities. While the overall morphology is qualitatively similar across configurations, the surface roughness appears to increase with inter-pulse delay. This qualitative observation is supported by

Table 1
Comparison of final-state observables for Cu and steel. The effective penetration depth d_{eff}, scanning ablation threshold fluence Φ_{thr}, and maximum ablation efficiency η_{abl} are listed for different inter-pulse delays in the double-pulse configuration, as well as for the single-pulse configuration.

	Cu			Stainless steel AISI304		
δ_t	d_{eff} [nm]	Φ_{thr} [J/cm^2]	Maximum η_{abl} [μm^3/μJ]	d_{eff} [nm]	Φ_{thr} [J/cm^2]	Maximum η_{abl} [μm^3/μJ]
Single-pulse	(16 ± 1)	(0.73 ± 0.02)	(2.32 ± 0.04)	(4 ± 1)	(0.18 ± 0.01)	(2.03 ± 0.06)
12.2 ns	(5 ± 1)	(0.62 ± 0.03)	(0.93 ± 0.05)	(3 ± 1)	(0.21 ± 0.01)	(1.80 ± 0.07)
122 ns	(13 ± 1)	(0.65 ± 0.02)	(1.90 ± 0.04)	(4 ± 1)	(0.19 ± 0.01)	(2.24 ± 0.08)
231.8 ns	(17 ± 1)	(0.72 ± 0.03)	(2.52 ± 0.03)	(4 ± 1)	(0.19 ± 0.01)	(2.27 ± 0.08)

quantitative surface roughness analysis using white-light interferometric microscopy, revealing an increase in the root-mean-square roughness S_q from 0.26 μm at $\delta_t = 12.2$ ns to 0.42 μm at 231.8 ns. The highest roughness of 0.455 μm is observed for the single-pulse configuration.

3.1.2. Steel

The ablation depths and efficiencies for steel are shown in Fig. 2. As shown in Fig. 2a, the ablation depths for steel are approximately a factor of four lower than those observed for Cu across the investigated peak fluence range. As in the case of Cu, two distinct ablation regimes are observed: the low-fluence spallation regime, followed by a transition to the phase explosion regime at a peak fluence of approximately 0.6 J/cm^2, which is lower than the corresponding transition fluence of approximately 2 J/cm^2 observed for Cu. For steel, this transition is considerably less pronounced than for Cu, as the change in slope between the two regimes is more gradual. The ablation scanning threshold fluence and effective penetration depth were determined by fitting Eq. (3) only to the data below a peak fluence of 0.6 J/cm^2, yielding an approximately constant scanning threshold fluence of 0.2 J/cm^2 that is independent of the inter-pulse delay (see Table 1). The effective energy penetration depth increases slightly with inter-pulse delay, from 3 nm at $\delta_t = 12.2$ ns to 4 nm at $\delta_t = 231.8$ ns, where it matches the value obtained for the single-pulse configuration (see Table 1).

When considering the ablation efficiency for steel (Fig. 2b), the overall trend appears largely independent of the inter-pulse delay. In all cases, the ablation efficiency η_{abl} increases with fluence, reaches a maximum at approximately $\Phi_0 = 3 \bullet \Phi_{thr}$, and then decreases at higher fluences. For an inter-pulse delay of $\delta_t = 12.2$ ns, the maximum ablation efficiency is approximately 1.8 μm^3/μJ. This is about 20% lower than the corresponding maximum of 2.27 μm^3/μJ observed for a longer inter-pulse delay of 231.8 ns (see Table 1). These values exceed the maximum efficiency of 2.03 μm^3/μJ obtained in the single-pulse configuration by approximately 12%. Notably, the maximum single-pulse configuration efficiency for steel is approximately 13% lower than that for Cu, which reaches a value of 2.32 μm^3/μJ under identical conditions.

The corresponding SEM images of the laser-processed steel surfaces at a fixed peak fluence of $\Phi_0 = 3.0 \bullet \Phi_{thr}$ are shown in Fig. 2c. As for Cu, this peak fluence was selected because here the maximum ablation efficiency is observed (see Fig. 2b). All surfaces exhibit regular, periodic features that are consistent with the formation of laser-induced periodic surface structures (LIPSS) [30]. However, at the shortest inter-pulse delay of 12.2 ns, these periodic structures are partially obscured by large, irregular surface features such as deep pits and elevated bumps, suggesting a rougher morphology. This qualitative observation is supported by white-light interferometric surface roughness measurements, which reveal a root-mean-square roughness S_q of 0.32 μm at $\delta_t = 12.2$ ns, decreasing to 0.25 μm at 231.8 ns. The lowest roughness of 0.23 μm is observed for the single-pulse configuration.

3.1.3. Comparison between copper and steel

Comparing the maximum ablation efficiencies for Cu (Fig. 1b) and steel (Fig. 2b), clear differences emerge in the sensitivity to the inter-pulse delay (see Table 1). For Cu, the ablation efficiency decreases by approximately 60% when the delay is reduced from 231.8 ns to 12.2 ns, whereas for steel the corresponding reduction is only about 20%. In addition, for steel the ablation efficiency level for the single-pulse configuration is reached at $\delta_t = 122.0$ ns, while for Cu the ablation efficiency remains below the single-pulse configuration efficiency at this delay. In contrast, the surface morphology exhibits inverse trends: for Cu, the surface roughness increases with inter-pulse delay (Fig. 1c), whereas for steel it decreases (Fig. 2c), with the roughest surface observed at $\delta_t = 12.2$ ns, and the smoothest in the single-pulse configuration.

3.2. Comparing double-pulse ablation dynamics with single-pulse transient reflectance change

To better understand the inter-pulse-delay dependence of ablation efficiency observed in the double-pulse experiments, single-pulse PPM measurements were performed to probe the ablation plume state at the time of second-pulse arrival under comparable irradiation conditions. While special care was taken to keep the pulse duration and beam waist radius constant between the double-pulse (see Section 2.2) and single-pulse PPM experiments (see Section 2.3), differences in the experimental setups remain. First, the incidence angle of the laser pulses was 0° in the double-pulse experiments and 35° in the PPM experiments. Second, the double-pulse experiments were conducted with a total of 1536 pulses per position, while the PPM experiments were performed in single-pulse mode. These differences in incidence angle and surface condition affect the absorption of the laser pulse [37], particularly due to incubation effects in the double-pulse configuration, where each pulse interacts with a surface modified by preceding pulses [38]. To account for these differences and allow for a meaningful comparison between the double-pulse and PPM experiments, the following analysis is performed at the same multiples of the respective ablation threshold fluence [19].

For the double-pulse configuration, the scanning ablation threshold fluence determined at an inter-pulse delay of $\delta_t = 231.8$ ns was used for normalization, as both the scanning ablation threshold fluence and the ablation efficiency reach a stable plateau at this delay (see Table 1 and Supplementary Information Sections S1 for Cu and S2 for steel). For the PPM measurements, the single-pulse ablation threshold fluences were determined as (2.0 ± 0.1) J/cm^2 for Cu and (0.18 ± 0.01) J/cm^2 for steel using the D^2-method [39] (see Supplementary Information, Section S3).

Two multiples of the ablation threshold fluence were selected for comparison between the two experiments. A peak fluence of $1.5 \bullet \Phi_{thr}$ was chosen as it lies well within the spallation regime where Eq. (3) applies. In addition, a peak fluence of $3.0 \bullet \Phi_{thr}$ was chosen, as the maximum ablation efficiency is approximately reached at this value regardless of the inter-pulse delay and material (see Fig. 1b for Cu and Fig. 2b for steel).

3.2.1. Copper

The ablation efficiency for Cu shows a pronounced dependence on the inter-pulse delay, as illustrated in Fig. 3a. For both investigated peak fluences, η_{abl} increases with increasing inter-pulse delay δ_t. At $\Phi_0 = 1.5 \bullet \Phi_{thr}$, the efficiency rises steeply up to $\delta_t = 122.0$ ns, where it approximately equals the single-pulse configuration value of 1.7 μm^3/μJ (solid black line). Beyond this point, the increase flattens, reaching a

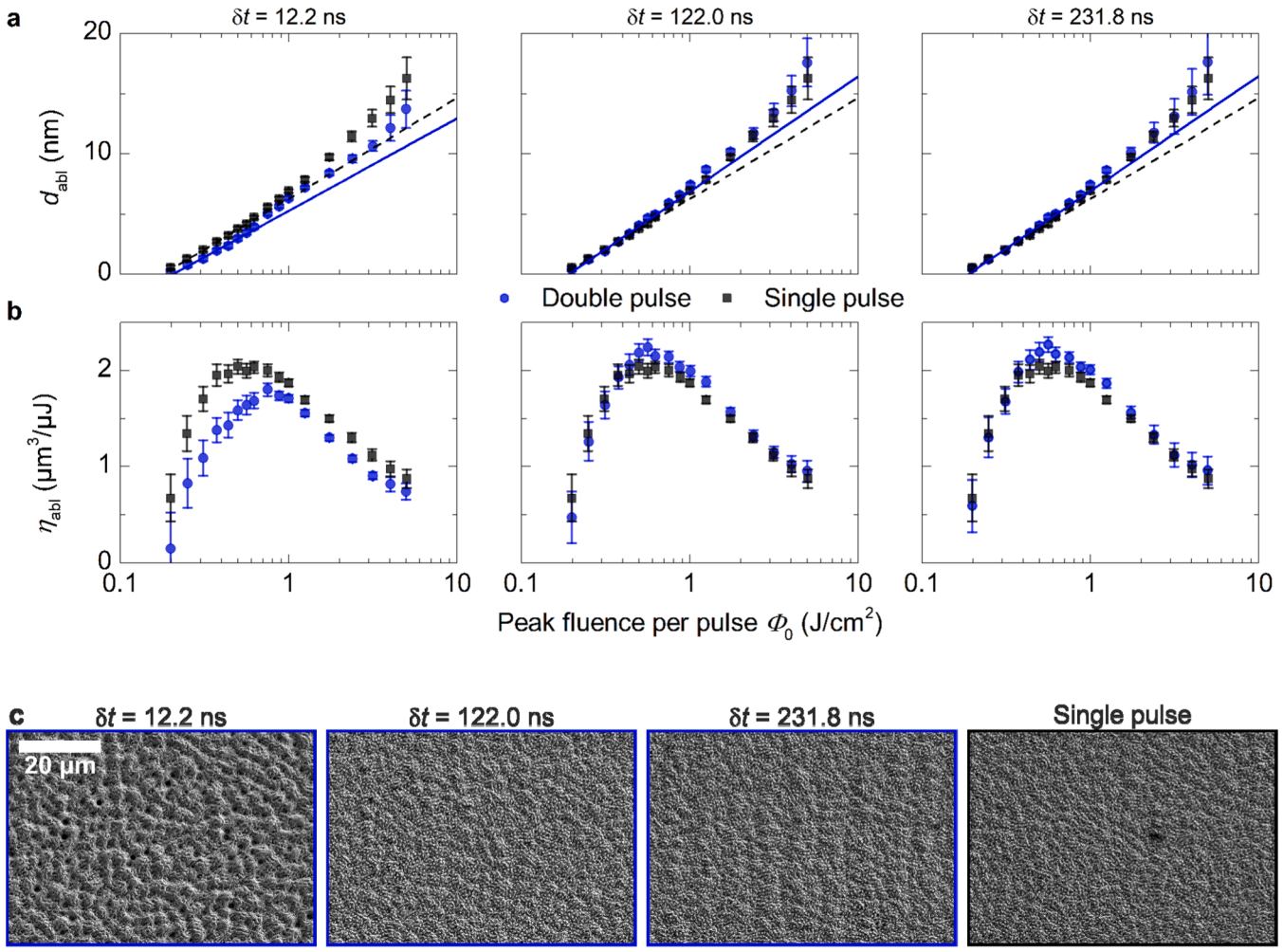

Fig. 2. Final-state ablation characteristics of steel processed using the double-pulse and single-pulse configurations. In both cases, the laser emitted pulses with a duration of 10 ps (FWHM) and a central wavelength of 1064 nm. In the double-pulse configuration, each emission event consisted of two energetically equal pulses separated by an inter-pulse delay δ_t, whereas in the single-pulse configuration each emission event consisted of a single pulse. The emission events were spaced by 5 µs, and the total number of incident pulses per position was 1536 in both configurations. Inter-pulse delays of 12.2 ns (left column), 122.0 ns (middle column), and 231.8 ns (right column) are shown. a) Ablation depth per pulse d_{abl} as a function of incident peak fluence per pulse Φ_0. The scanning ablation threshold fluences Φ_{thr} were determined by fitting Eq. (3) to the data in the spallation regime for peak fluences $\Phi_0 < 0.6$ J/cm^2. For the double-pulse configuration the obtained fits are shown by solid red lines, whereas for the single-pulse configuration the fits are shown by dashed black lines. b) Ablation efficiency η_{abl} as a function of Φ_0. c) SEM images of the surface morphology after laser structuring at a fixed peak fluence of $\Phi_0 = 3.0 \bullet \Phi_{thr}$, corresponding approximately to the peak fluence at which the maximum ablation efficiency is reached in the single-pulse configuration. Images are shown for three different inter-pulse delays in the double-pulse configuration (12.2 ns, 122.0 ns, and 231.8 ns), as well as for the single-pulse configuration. The scale bar in the left image applies to all images. The ablation depths and surface morphologies were evaluated in the central region of the 1 mm x 1 mm scanned squares and are representative of the surface morphology within the processed area.

value of 1.9 µm^3/µJ at $\delta_t = 231.8$ ns, which is about 12% higher than the single-pulse configuration value. For $\Phi_0 = 3.0\ \Phi_{thr}$, η_{abl} increases continuously throughout the entire inter-pulse delay range, reaching a value of approximately 2.5 µm^3/µJ at $\delta_t = 231.8$ ns. This corresponds to an increase of roughly 14% compared to the single-pulse configuration value of 2.2 µm^3/µJ, shown by the dashed black line in Fig. 3a.

Contour plots depicting PPM measurements of the transient reflectance change $\Delta R/R_0$ are shown in Fig. 3b for incident peak fluences of $1.5 \bullet \Phi_{thr}$ and $3.0 \bullet \Phi_{thr}$. For both peak fluences, $\Delta R/R_0$ drops rapidly following pump-pulse impact at $\Delta t = 0$ ns. In the first few picoseconds, this drop is dominated by the density decrease at the material's surface, which progresses more rapidly at higher fluence [21]. Starting from approximately 0.1 ns, the relative reflectance saturates at a value close to $\Delta R/R_0 \approx -1$, indicating that nearly all of the incoming probe pulse is absorbed or scattered. This vanishing reflectance originates from the formation of a dense ablation plume within the phase explosion regime [19,40,41], consisting of individual atoms and atom clusters as well as liquid droplets [6]. The lateral extent of the region with $\Delta R/R_0 \approx -1$ spans approximately 6 µm for $\Phi_0 = 1.5 \bullet \Phi_{thr}$ and 12 µm for $\Phi_0 = 3.0 \bullet \Phi_{thr}$, covering nearly the full diameter of the ablation crater. Additionally, for $\Phi_0 = 3.0 \bullet \Phi_{thr}$ an outward-propagating stripe of increased reflectance is observed between 0.1 ns and 4 ns, which indicates the emission of a shockwave into the surrounding air and highlights the enhanced expansion of the ablation plume compared to a peak fluence of $1.5 \bullet \Phi_{thr}$. Following this, the reflectance gradually recovers, starting from $\Delta t = 12$ ns and $\Delta t = 5$ ns for $\Phi_0 = 1.5 \bullet \Phi_{thr}$ and $3.0 \bullet \Phi_{thr}$, respectively. Aside from minor reflectance fluctuations in the central region, the spatial reflectance profile begins to resemble the final state (marked as "inf" in Fig. 3b), suggesting that the ablation plume becomes fully transparent between delay times of 50 ns and 100 ns. Overall, the transient reflectance response differs only slightly between the two applied peak fluences, indicating a typical photothermal ablation mechanism in both cases.

The final-state reflectance ($\Delta t =$ inf in Fig. 3b) remains significantly reduced even after full plume dissipation. This persistent reflectance decrease, approximately down to −0.3, can be attributed to the surface

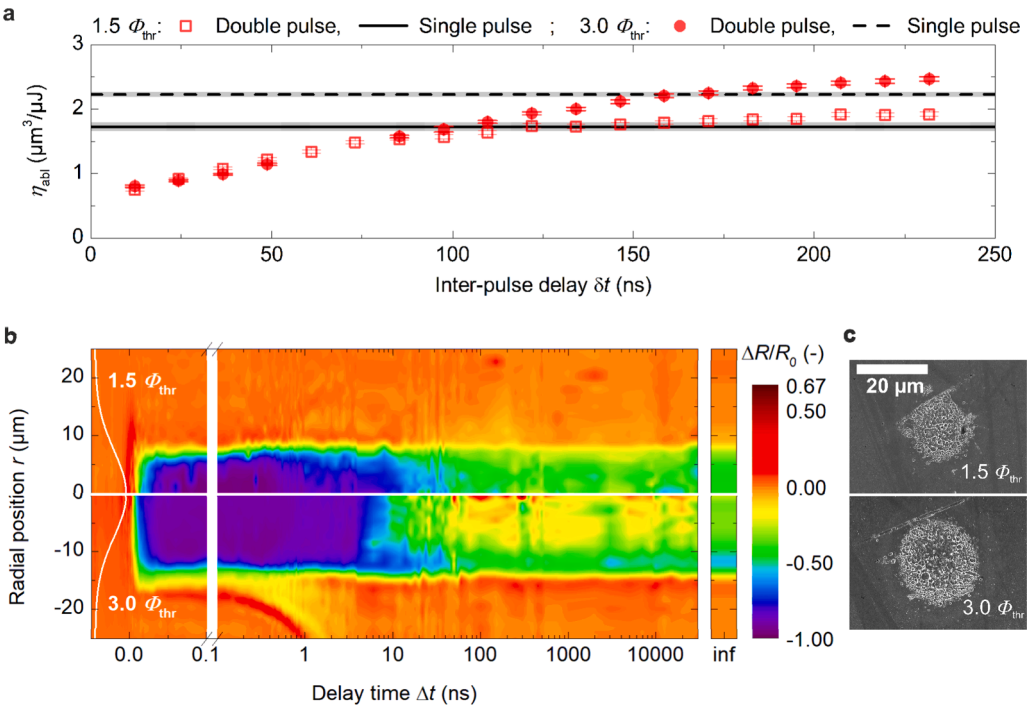

Fig. 3. Comparison of double-pulse and single-pulse experiments on Cu using laser pulses with a duration of 10 ps. a) Ablation efficiency η_{abl} as a function of inter-pulse delay δ_t for incident peak fluences of $\Phi_0 = 1.5\ \Phi_{thr}$ (open red squares) and $\Phi_0 = 3.0\ \Phi_{thr}$ (filled red circles). Solid and dashed black lines indicate the ablation efficiency measured in the single-pulse configuration for $1.5\bullet\Phi_{thr}$ and $3.0\bullet\Phi_{thr}$, respectively. The gray shaded areas denotes the corresponding standard deviation. b) Transient relative reflectance change $\Delta R/R_0$ following a single pump pulse, measured as a function of delay time Δt and radial position r for $\Phi_0 = 1.5\bullet\Phi_{thr}$ (top half) and $\Phi_0 = 3.0\bullet\Phi_{thr}$ (bottom half). The white curve denotes the spatial Gaussian fluence distribution. The final state reflectance (marked with "inf" in a separate panel) was measured 1 s after pump pulse arrival. c) SEM images of single-pulse ablation craters generated at $\Phi_0 = 1.5\bullet\Phi_{thr}$ (top) and $\Phi_0 = 3.0\bullet\Phi_{thr}$ (bottom). The scale bar applies to both images.

morphology generated by the ablation process. As seen in the corresponding SEM images of single-pulse craters in Fig. 3c, rough crater structures with irregular edges and lateral dimensions in the micrometer range are observed for both peak fluences. The increased surface roughness enhances scattering and absorption of the probe light [37], which explains the lowered reflectance compared to the pristine surface.

3.2.2. Steel

The dependence of the ablation efficiency η_{abl} on the inter-pulse delay for steel is shown in Fig. 4a. For a peak fluence of $1.5\bullet\Phi_{thr}$ the ablation efficiency increases from 0.83 $\mu m^3/\mu J$ at $\delta_t = 12.2$ ns to 1.1 $\mu m^3/\mu J$ at $\delta_t = 24.4$ ns. Following this an approximately constant ablation efficiency is observed up until the longest investigated inter-pulse delay of 231.8 ns. At this point, the ablation efficiency of 1.3 $\mu m^3/\mu J$ approximately equals the single-pulse configuration value of 1.35 $\mu m^3/\mu J$ (see black solid line in Fig. 4a). At a peak fluence of $3.0\bullet\Phi_{thr}$ the general ablation efficiency trend is comparable to that observed for $1.5\bullet\Phi_{thr}$. However, a constant level of approximately 2.2 $\mu m^3/\mu J$ is reached only at an inter-pulse delay of 36.6 ns, with decreased ablation efficiency for smaller inter-pulse delays. Furthermore, starting from an inter-pulse delay of 36.6 ns, double-pulse processing results in an increased ablation efficiency (2.2 $\mu m^3/\mu J$) compared to the single-pulse configuration ablation efficiency of 2.0 $\mu m^3/\mu J$ (see black dashed line in Fig. 4c).

The transient relative reflectance change $\Delta R/R_0$ depicted in Fig. 4b reveals two distinct ablation regimes depending on the incident peak fluence. At $1.5\bullet\Phi_{thr}$, a reflectance drop to approximately $\Delta R/R_0 = -0.85$ is observed at $\Delta t = 0.15$ ns. As in the case of Cu, this decrease is attributed to a rapid density decrease at the material surface [21]. Between $\Delta t = 0.15$ ns and $\Delta t = 1.2$ ns, the reflectance exhibits oscillations. These Newton rings arise from interference between a propagating spallation layer and the stationary material beneath it and serve as experimental evidence for material ejection via photomechanical spallation [21,41,42]. A recovery of the reflectance begins around $\Delta t = 2$ ns, and the final state is reached at approximately $\Delta t = 100$ ns. At $3.0\bullet\Phi_{thr}$, the initial drop in reflectance is both faster and more pronounced, reaching $\Delta R/R_0 \approx -1$ already at $\Delta t = 0.05$ ns. This indicates the formation of a dense, highly absorbing and scattering ablation plume, characteristic of photothermal material ejection within the phase explosion regime [19,40,41]. In this case, material is expelled more rapidly, and the reflectance starts to recover as early as $\Delta t = 0.2$ ns, with the final reflectance state reached by $\Delta t \approx 50$ ns.

The final-state ablation craters for single-pulse processing (Fig. 4c) exhibit sharp edges with smooth surfaces for both peak fluences. In contrast to Cu, the generated craters closely resemble the pristine surface in terms of roughness. As a result, the final-state reflectance ($\Delta t =$ inf in Fig. 4b) remains nearly unchanged, with values that are within a few percent of the initial reflectance prior to laser irradiation.

4. Discussion

4.1. Normalized second-pulse efficiency and plume transmittance as diagnostic quantities

To assess how interaction between the second pulse and the ablation plume affects ablation efficiency, we introduce a diagnostic quantity that isolates the contribution of the second pulse in the double-pulse configuration. The contribution of the second pulse to the ablation efficiency is estimated by subtracting the first-pulse contribution from the total measured efficiency in the double-pulse configuration. To do so, the ablation efficiency of the first pulse in the double-pulse configuration must be estimated separately. This estimate is obtained from the single-pulse configuration, in which single pulses are spaced by an inter-pulse delay of 5 μs. Pump–probe microscopy confirms that the ablation

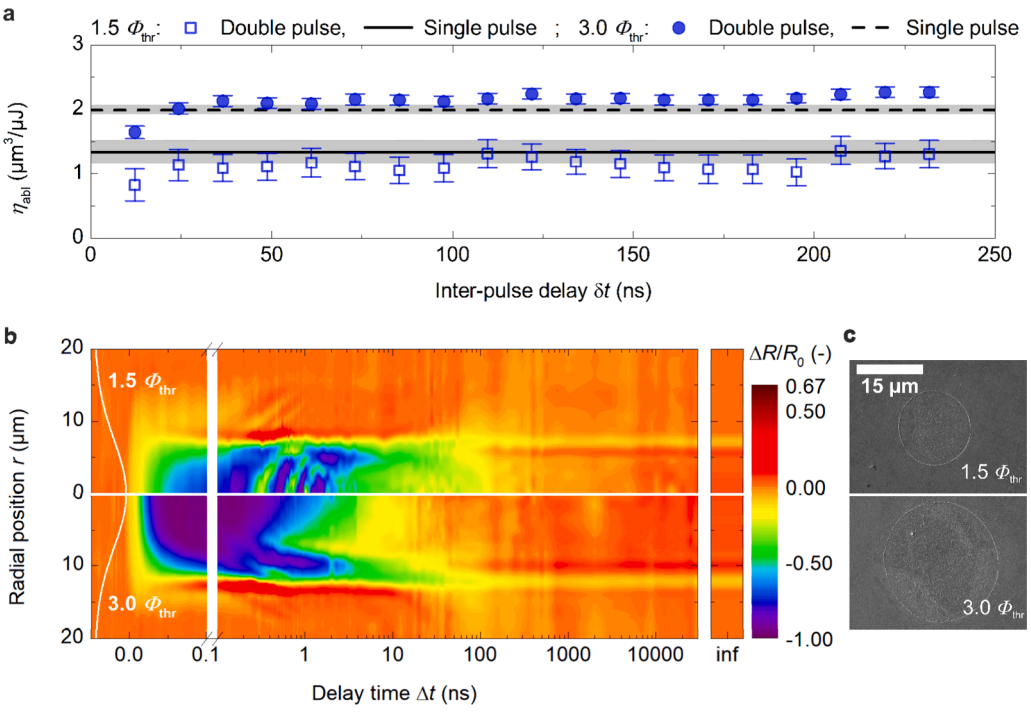

Fig. 4. Comparison of double-pulse and single-pulse experiments on steel using laser pulses with a duration of 10 ps. a) Ablation efficiency η_{abl} as a function of inter-pulse delay δ_t for incident peak fluences of $\Phi_0 = 1.5\ \Phi_{thr}$ (open blue squares) and $\Phi_0 = 3.0\ \Phi_{thr}$ (filled blue circles). Solid and dashed black lines indicate the ablation efficiency measured in the single-pulse configuration for $1.5\bullet\Phi_{thr}$ and $3.0\bullet\Phi_{thr}$, respectively. The gray shaded areas denotes the corresponding standard deviation. b) Transient relative reflectance change $\Delta R/R_0$ following a single pump pulse, measured as a function of delay time Δt and radial position r for $\Phi_0 = 1.5\bullet\Phi_{thr}$ (top half) and $\Phi_0 = 3.0\bullet\Phi_{thr}$ (bottom half). The white curve denotes the spatial Gaussian fluence distribution. The final state reflectance (marked with "inf' in a separate panel) was measured 1 s after pump pulse arrival. c) SEM images of single-pulse ablation craters generated at $\Phi_0 = 1.5\bullet\Phi_{thr}$ (top) and $\Phi_0 = 3.0\bullet\Phi_{thr}$ (bottom). The scale bar applies to both images.

plume has dissipated before the arrival of the next pulse at this delay (see Fig. 3 for Cu and Fig. 4 for steel), ensuring that interaction with the ablation plume is avoided. Since both the single-pulse and double-pulse configuration deliver the same total number of pulses per position, we approximate the first-pulse contribution in the double-pulse configuration as half the ablation efficiency η_{SP} measured in the single-pulse configuration. Subtracting this value from the total double-pulse efficiency η_{DP} yields the ablation efficiency of the second pulse. To evaluate how strongly this second pulse efficiency is affected by interaction with the ablation plume, its efficiency is normalized by half the single-pulse configuration value. This yields the normalized second-pulse ablation efficiency η_{norm}, defined by Equation43.

$$\eta_{norm} = \frac{\eta_{DP} - \frac{1}{2}\eta SP}{\frac{1}{2}\eta SP} \tag{4}$$

This dimensionless quantity expresses how effectively the second pulse ablates material compared to a non-interacting pulse. Based on its value, four interaction regimes are distinguished:

- $\eta_{norm} < 0$: Redeposition regime – the total ablated volume is reduced compared to the first pulse alone, implying that the second pulse adds material to the surface rather than removing it.
- $0 \leq \eta_{norm} < 1$: Shielding regime – the second pulse removes less material than a pulse that does not interact with the ablation plume.
- $\eta_{norm} \approx 1$: Recovery regime – the second pulse ablates with the same efficiency as a non-interacting pulse.
- $\eta_{norm} > 1$: Enhancement regime – the second pulse removes more material than a non-interacting pulse.

To interpret the η_{norm} trends, it is essential to understand how strongly the ablation plume attenuates the second pulse. Absorption and scattering within the plume reduce the energy that reaches the target surface, thereby decreasing the ablation efficiency. To quantify this shielding effect, we introduce the optical plume transmittance T_P, which is derived from the PPM measurements and describes the fraction of pulse energy transmitted through the evolving plume, accounting for attenuation due to both absorption and scattering within the plume.

As the probe pulse traverses the ablation plume, reflects off the sample surface, and exits the plume again, the total measured reflectance $R(\Delta t)$ is given by Eq. (5).

$$R(\Delta t) = T_P(\Delta t) \cdot R_S(\Delta t) \cdot T_P(\Delta t) \tag{5}$$

Here $R_S(\Delta t)$ denotes the reflectance of the sample surface located beneath the ablation plume.

To extract the plume transmittance $T_P(\Delta t)$ from Equation 5, the surface reflectance beneath the plume $R_S(\Delta t)$ must be known. This reflectance may vary temporally due to three effects: (1) temperature-dependent optical properties [43], (2) transient melting [44], and (3) transient morphological changes of the surface [37].

Literature data on ultrafast laser excitation of Ni, which has a thermal conductivity of 90.7 W/(m•K) [45], report solidification within 5 ns after pulse impact at peak fluences up to $3\bullet\Phi_{thr}$ [46]. Given the significantly higher thermal conductivity of 401 W/(m•K) [45] for Cu, it is expected to solidify even more rapidly, likely well before the shortest investigated inter-pulse delay of 12.2 ns. Consequently, reflectance changes due to an elevated surface temperature or the presence of a transient liquid phase are excluded for Cu. However, Cu develops pronounced surface roughness following ablation (see Fig. 3c), resulting in a reduced reflectance (see Fig. 3b). As solidification is expected to occur well before the shortest investigated inter-pulse delay of 12.2 ns, it is assumed that these surface features are already fully formed at this delay time and do not evolve further.

For steel, the low thermal conductivity of 14 W/(m•K) [47] suggests that transient melting may persist longer than in Cu. However, for FeNi

alloys, reflectance is largely unaffected by temperature and the solid–liquid phase transition at the probe wavelength of 520 nm [43], and SEM images (Fig. 4c) confirm a flat ablation morphology with no significant surface roughness. As a result, both melting and morphological effects can be considered negligible for the evolution of $R_S(\Delta t)$ in steel.

Based on this analysis, the surface reflectance beneath the plume is approximated using the reflectance measured at the longest inter-pulse delay in the PPM experiments: $R_S(\Delta t) \approx R(250\ \text{ns})$. At this delay, the ablation plume has dissipated (see Fig. 3b for Cu and Fig. 4b for steel), and the surface is assumed to be fully solidified and stable. The transient plume transmittance is thus calculated by Eq. (6).

$$T_P(\Delta t) = \left(\frac{R(\Delta t)}{R(\Delta t = 250ns)}\right)^{\frac{1}{2}} \tag{6}$$

The reflectance R is related to the measured relative reflectance change $\Delta R/R_0$ by $R = (\Delta R/R_0 + 1)\cdot R_0$ (see Eq. (2)), where R_0 is the reflectance of the pristine surface. Substituting this into Eq. (6) yields

$$T_P(\Delta t) = \left(\frac{\Delta R/R_0(\Delta t) + 1}{\Delta R/R_0(\Delta t = 250ns) + 1}\right)^{\frac{1}{2}} \tag{7}$$

such that the dependence on the absolute value of R_0 cancels. The plume transmittance is therefore determined exclusively from the experimentally measured relative reflectance changes, without requiring any assumption about the absolute surface reflectance. Since the ablation plume extends across the full ablation area, spatial averaging was performed from $r = 0$ µm to $r = r_{abl}$ for each delay time Δt. Here r_{abl} is the ablation radius determined as described in Section S3 of the Supplementary Information.

An additional issue arises when directly comparing the ablation plume transmission obtained from the PPM experiments and the double-pulse ablation efficiency. The transient reflectance and hence, the ablation plume transmittance was measured at a wavelength of 528 nm, while the double-pulse experiments were carried out at 1064 nm.

To resolve this issue, the following steps were taken. It is reasonable to assume that the ablation plume consists of a plasma with an approximate temperature of 10 kK [48] and density smaller than the critical density of about $1\bullet10^{21}$ cm^{-3} at 1064 nm and $4\bullet10^{21}$ cm^{-3} at 528 nm [49]. By approximating the plasma's optical properties by a simple Drude model, it can be shown (see detailed derivation in Supplementary Information, Section S4) that the ablation plume transmittance at 1064 nm can be approximated from the measured plume transmittance at 528 nm by:

$$T_P(1064nm) \approx T_P(528nm)^4 \tag{8}$$

Eq. (8) allows comparing the transient ablation plume transmittance at 1064 nm with the normalized second-pulse efficiency η_{norm} at 1064 nm.

4.2. Correlation of plume transmittance and normalized second-pulse efficiency

This section investigates how the normalized second-pulse efficiency η_{norm} correlates with the plume transmittance T_P. The goal is to assess whether the transient optical properties of the ablation plume, quantified by T_P, can explain the delay-dependent trends observed in the ablation efficiency of the second pulse. Fig. 5 presents both quantities for Cu and steel at peak fluences of $1.5\bullet\Phi_{thr}$ and $3.0\bullet\Phi_{thr}$, providing the basis for the following analysis.

For Cu at $1.5\bullet\Phi_{thr}$ (Fig. 5, top left), η_{norm} closely follows the evolution of T_P, rising within the same temporal window up to approximately 100 ns. This trend indicates that shielding by the ablation plume is the primary mechanism limiting second-pulse efficiency at inter-pulse delays below 100 ns. Beyond 100 ns, η_{norm} reaches unity, consistent with the near-complete recovery of plume transmittance, allowing the second pulse to reach the Cu surface without significant plume absorption losses. At longer delays, η_{norm} exceeds 1, implying that the second pulse becomes more effective than a single pulse once the plume has cleared. At the shortest inter-pulse delay (12.2 ns), η_{norm} briefly drops below zero, indicating minor redeposition. While this effect remains small at $1.5\bullet\Phi_{thr}$, at a peak fluence of $3.0\bullet\Phi_{thr}$ (Fig. 5, top right), redeposition becomes strongly pronounced for inter-pulse delays below 50 ns,

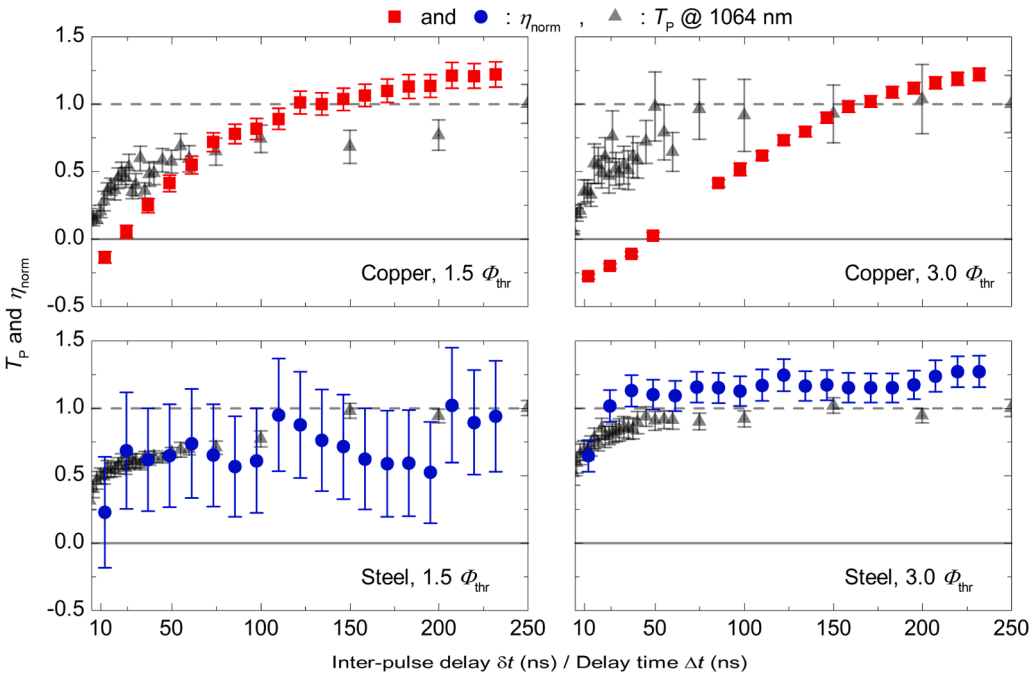

Fig. 5. Normalized second-pulse efficiency η_{norm} and plume transmittance T_P at a pulse duration of 10 ps for Cu (top row) and steel (bottom row), shown as a function of inter-pulse delay δ_t and probe-pulse delay time Δt, respectively. Results are shown for $1.5\bullet\Phi_{thr}$ (left column) and $3.0\bullet\Phi_{thr}$ (right column). Red squares and blue circles denote $\eta_{norm}(\delta_t)$ for Cu and steel, respectively. Grey triangles show the plume transmittance $T_P(\Delta t)$ at 1064 nm, approximated from transient reflectance data using Eq. (8). Two critical values of $\eta_{norm} = 0$ and $\eta_{norm} = 1$ are highlighted by solid and dashed horizontal lines, respectively.

coinciding with the region of lowest plume transmittance. At this high fluence, the ablation plume contains a significantly higher vapor fraction compared to the lower-fluence regime. The second pulse is absorbed within the vapor above the surface, leading to recoil-pressure-driven redeposition of ablated material [11,20,22–24], which explains the observed negative η_{norm} values. Interestingly, while T_P recovers rapidly beyond 50 ns, η_{norm} only reaches unity around 150 ns, suggesting that the redeposition effect may partially persist even after the plume becomes optically transparent. In this regime, the second pulse reaches the target and causes ablation, but part of the ablated material may be pushed back toward the surface and redeposited, even if the net removed volume remains positive. Nevertheless, the strongest suppression of second-pulse efficiency once again correlates with the lowest plume transmittance, and enhanced efficiency ($\eta_{norm} > 1$) is again observed once the plume becomes fully transparent.

For steel at 1.5•Φ_{thr} and 3.0•Φ_{thr} (Fig. 5, bottom row), η_{norm} and T_P show a strong correlation across the entire delay range. No negative η_{norm} values are observed, indicating that redeposition does not occur in the investigated range. Shielding by the ablation plume is the sole mechanism limiting second-pulse efficiency, and its effects are confined to the shortest delay of 12.2 ns. Notably, the suppression is more pronounced at the lower fluence of 1.5•Φ_{thr}, with η_{norm} dropping to approximately 0.25 at an inter-pulse delay of 12.2 ns, compared to about 0.5 at the same delay for 3.0•Φ_{thr}. Beyond this point, the plume rapidly clears. This is particularly evident at 3.0•Φ_{thr}, where the recovery of plume transmittance to unity coincides with the recovery of η_{norm} to 1. These observations confirm that shielding is the dominant mechanism affecting inter-pulse delay dependent efficiency in steel, establishing T_P as a diagnostic for plume-shielding-induced reductions of ablation efficiency in steel.

Comparing Cu and steel, several material-specific characteristics help explain the observed differences in plume transmittance and normalized second-pulse efficiency. First, the ablation depth per pulse is significantly higher for Cu. As shown in Table 1, Cu exhibits an approximately fourfold increase in ablation depth compared to steel at the same multiple of the ablation threshold fluence. This implies that the plume generated by the first pulse in Cu contains substantially more ablated material, resulting in a denser and more optically opaque plume. This interpretation is consistent with the overall lower plume transmittance and longer recovery times observed for Cu relative to steel. In contrast, the lower ablation depth and decreased plume density for steel likely contribute to faster plume vanishing, reduced shielding and absence of redeposition.

Second, the dominant ablation mechanisms differ between the two materials. Cu shows consistent signatures of photothermal ablation with characteristics of phase explosion across both fluence regimes (Fig. 3), generating a plume composed of atoms, clusters, and droplets, all highly effective at attenuating the second pulse [19]. For steel, however, the ablation mechanism transitions with fluence (Fig. 4): at 1.5•Φ_{thr}, photomechanical spallation dominates, producing spallation layers with lower optical absorption; at 3.0•Φ_{thr}, indications of phase explosion appear, yet the plume remains less absorptive than in Cu. This is reflected in the faster recovery of both T_P and η_{norm} for steel in the high-fluence regime, despite entering a similar ablation regime.

Across both materials, increasing the peak fluence shortens the duration of plume-induced shielding, as seen in the faster recovery of T_P at 3.0•Φ_{thr} compared to 1.5•Φ_{thr}. However, the corresponding recovery in η_{norm} is notably slower for Cu at high fluence. This discrepancy indicates a breakdown of the T_P–η_{norm} correlation in regimes where dense vapor-mediated shielding dominates the second-pulse interaction. One contributing factor may be that plume transmittance in the current experiments is inferred from single-pulse PPM measurements, which do not account for how plume dynamics might evolve when the surface was already irradiated by multiple pulses. In addition, for Cu at 3.0•Φ_{thr}, where the densest plume is inferred from the lowest T_P values, the assumption of a maximum plasma density of $n_0 = 10^{20}$ 1/cm^3, used to convert the transmittance at the probe wavelength of 528 nm used in the PPM experiments to the wavelength of 1064 nm used in the double-pulse experiments (see Supplementary Information, Section S4), may no longer be valid under such conditions. These limitations may contribute to the pronounced mismatch between T_P and η_{norm} for Cu at a peak fluence of 3.0•Φ_{thr}.

In summary, plume transmittance derived from single-pulse PPM data provides a robust diagnostic for understanding second-pulse efficiency trends in shielding-dominated regimes. While deviations occur at high fluence in Cu due to dense vapor plumes and redeposition, the good agreement in all other cases, including steel across both fluences, highlights the utility of T_P for probing ultrafast laser-plume interactions and predicting double-pulse ablation efficiency.

4.3. Enhancement of ablation efficiency at long inter-pulse delays

Efficiency enhancement, indicated by η_{norm} values exceeding unity, is observed for both Cu and steel once the ablation plume has fully cleared and plume transmittance has returned to unity. The enhancement amounts to up to 9% for Cu and up to 12% for steel (see Table 1). Efficiency enhancements of this magnitude are consistent with previously reported MHz-burst ablation studies on Cu at comparable inter-pulse delays of 15.5 ns, where an efficiency increase on the order of 10% to 15% relative to single-pulse ablation was observed when operating with a 3-pulse burst. Based on the present measurements, a potential contribution from surface morphology changes to this efficiency increase can be ruled out. As shown in Fig. 1 for Cu and Fig. 2 for steel, the surface morphology after double-pulse irradiation at $\delta_t = 122$ ns closely resembles that of the single-pulse case, as evident from the SEM images. This suggests that increased surface roughness, which enhances absorptance [37] and facilitates incubation [50], is not responsible for the observed efficiency enhancement.

A more plausible explanation is heat accumulation, where residual heat [10,51] from the first pulse remains within the material and contributes to the energy budget of the second pulse. This effect can enhance ablation efficiency, as part of the energy required for ablation is already stored in the system rather than lost via heat dissipation [52,53]. The stronger enhancement observed for steel (12%) compared to Cu (9%) further supports this interpretation. Due to its lower thermal conductivity (90.7 W/(m•K) for steel versus 401 W/(m•K) for Cu), heat dissipates more slowly in steel, meaning more thermal energy remains in the irradiated volume by the time the second pulse arrives. As a result, heat accumulation contributes more strongly to ablation efficiency enhancement in steel than in Cu.

4.4. Practical implications: optimization of efficiency and surface quality

The results provide clear guidance for selecting optimal inter-pulse delays in double-pulse processing of Cu and steel. For Cu, inter-pulse delays shorter than 150 ns should be avoided due to pronounced redeposition and plume shielding, which significantly reduces second pulse efficiency. At delays exceeding 150 ns, ablation efficiency fully recovers and can even slightly exceed the single-pulse reference efficiency by up to 9% for Cu. Steel, in contrast, exhibits reduced plume shielding compared to Cu for inter-pulse delays below approximately 30 ns, but no evidence of redeposition. Once this inter-pulse delay is exceeded, double-pulse processing can yield a small efficiency increase of up to 12% for steel

Besides ablation efficiency, surface quality must also be considered in practical optimization. For Cu, a clear trend is observed: surface roughness increases from 0.2 μm to 0.4 μm as the inter-pulse delay increases. This increase may be explained by material redeposition. At short delays, redeposited material may partially fill holes or smooth the rough craters (Fig. 3c) formed by the first pulse, reducing surface roughness. Once the plume has dissipated and redeposition no longer occurs ($\delta_t > 50$ ns), roughness increases to values comparable to the

reference single-pulse ablation. For steel, no such smoothing effect is observed. Here surface quality remains largely unaffected by pulse timing, and double-pulse processing offers no clear benefit in terms of roughness control.

These results allow specific repetition rate recommendations for double-pulse processing. For Cu, inter-pulse delays of 150 ns or more enable efficient double-pulse ablation at repetition rates up to 6.7 MHz, by avoiding plume shielding. If reduced surface roughness is the primary goal, shorter delays and higher repetition rates may still be beneficial despite lower ablation efficiency. For steel, efficient double-pulse processing is achieved at inter-pulse delays of 30 ns or more, allowing repetition rates of up to 33 MHz.

Beyond the specific cases of Cu and steel, the material dependence of plume shielding observed here can be generalized qualitatively by considering the effective penetration depth of the deposited laser energy. This effective penetration depth increases with larger optical penetration depth, weaker electron–phonon coupling, and higher thermal conductivity, which together distribute the absorbed energy over a larger volume during the pulse [7]. Materials with a larger effective penetration depth therefore tend to exhibit higher ablation depths per pulse and generate denser, more optically opaque plumes, leading to stronger plume shielding and longer recovery times. Conversely, materials with more confined energy deposition are expected to produce less dense plumes and experience reduced shielding effects in double-pulse processing.

5. Conclusion

MHz-burst processing with ultrashort laser pulses offers a promising approach to harnessing the high pulse energies provided by modern laser systems. However, when inter-pulse delays are too short, significant reductions in ablation efficiency can occur due to plume shielding and, in some cases, redeposition of ablated material.

This study investigated these effects by combining double-pulse ablation experiments on Cu and steel with time-resolved pump–probe microscopy (PPM) measurements of plume transmittance. Inter-pulse delays between 12.2 ns and 231.8 ns were explored. The results show that plume shielding is the dominant mechanism limiting second-pulse efficiency in both materials, particularly at short delays. At 12.2 ns, efficiency reductions reach up to 63% in Cu and 21% in steel. In Cu, a dense vapor plume formed at high fluences also led to redeposition, causing negative second-pulse efficiencies.

As inter-pulse delay increases, these effects diminish. For Cu, full recovery of second-pulse efficiency occurs at delays exceeding 150 ns, corresponding to a maximum feasible repetition rate of approximately 6.7 MHz. For steel, recovery is already observed at inter-pulse delay exceeding 30 ns, allowing repetition rates up to 33 MHz. Processing at shorter delays remains possible but involves trade-offs between throughput, efficiency, and surface quality.

These findings establish temporal pulse shaping as a practical and tunable tool for optimizing ablation performance. By selecting appropriate inter-pulse delays, temporal pulse splitting allows high available peak fluences to be temporally distributed into the peak-fluence regime of maximum ablation efficiency, while avoiding plume-induced efficiency losses.

Statement

During the preparation of this work the authors used GPT-5.2 in order to improve language and readability. After using this tool, the authors reviewed and edited the content. The authors take full responsibility for the content of the publication.

CRediT authorship contribution statement

Maximilian Spellauge: Writing – original draft, Visualization, Methodology, Investigation, Data curation, Conceptualization. **David Redka:** Writing – original draft, Methodology, Investigation, Conceptualization. **Stefan Remund:** Writing – review & editing, Methodology, Investigation. **Beat Neuenschwander:** Writing – review & editing, Supervision, Project administration. **Heinz P. Huber:** Writing – review & editing, Supervision, Resources, Project administration. **Daniel.J. Förster:** Writing – review & editing, Investigation.

Declaration of competing interest

The authors declare that they have no known competing financial interests or personal relationships that could have appeared to influence the work reported in this paper.

Acknowledgements

The authors gratefully acknowledge funding from the Deutsche Forschungsgemeinschaft (DFG) under project numbers 428315411, 423531130 and 528706678.

Supplementary materials

Supplementary material associated with this article can be found, in the online version, at doi:10.1016/j.surfin.2026.109116.

Data availability

Data will be made available on request.

References

[1] S. Lei, X. Zhao, X. Yu, A. Hu, S. Vukelic, M.B.G. Jun, H.-E. Joe, Y.L. Yao, Y.C. Shin, Ultrafast laser applications in manufacturing processes: a State of the art review, J. Manuf. Sci. Eng. 142 (2020) 1–43, https://doi.org/10.1115/1.4045969.
[2] C. Momma, B.N. Chichkov, S. Nolte, F. von Alvensleben, A. Tünnermann, H. Welling, B. Wellegehausen, Short-pulse laser ablation of solid targets, Opt. Commun. 129 (1996) 134–142, https://doi.org/10.1016/0030-4018(96)00250-7.
[3] M. Domke, V. Matylitsky, S. Stroj, Surface ablation efficiency and quality of fs lasers in single-pulse mode, fs lasers in burst mode, and ns lasers, Appl. Surf. Sci. 505 (2020) 144594, https://doi.org/10.1016/j.apsusc.2019.144594.
[4] G. Raciukaitis, Ultra-short pulse lasers for microfabrication: a review, IEEE J. Sel. Top. Quant. Electron. 27 (2021) 1–12, https://doi.org/10.1109/JSTQE.2021.3097009.
[5] S. Nolte, C. Momma, H. Jacobs, A. Tünnermann, B.N. Chichkov, B. Wellegehausen, H. Welling, Ablation of metals by ultrashort laser pulses, J. Opt. Soc. Am. B. 14 (1997) 2716, https://doi.org/10.1364/JOSAB.14.002716.
[6] L.V. Zhigilei, Z. Lin, D.S. Ivanov, Atomistic modeling of short pulse laser ablation of metals: connections between melting, spallation, and phase explosion, J. Phys. Chem. C. 113 (2009) 11892–11906, https://doi.org/10.1021/jp902294m.
[7] J. Winter, M. Spellauge, J. Hermann, C. Eulenkamp, H.P. Huber, M. Schmidt, Ultrashort single-pulse laser ablation of stainless steel, aluminium, copper and its dependence on the pulse duration, Opt. Express 29 (2021) 14561, https://doi.org/10.1364/OE.421097.
[8] D. Redka, J. Winter, C. Gadelmeier, A. Djuranovic, U. Glatzel, J. Minár, H.P. Huber, Control of ultrafast laser ablation efficiency by stress confinement due to strong electron localization in high-entropy alloys, Appl. Surf. Sci. 594 (2022) 153427, https://doi.org/10.1016/j.apsusc.2022.153427.
[9] J. Furmanski, A.M. Rubenchik, M.D. Shirk, B.C. Stuart, Deterministic processing of alumina with ultrashort laser pulses, J. Appl. Phys. 102 (2007) 073112, https://doi.org/10.1063/1.2794376.
[10] B. Jäggi, D.J. Förster, R. Weber, B. Neuenschwander, Residual heat during laser ablation of metals with bursts of ultra-short pulses, Adv. Opt. Technol. 7 (2018) 175–182, https://doi.org/10.1515/aot-2018-0003.
[11] D.J. Förster, B. Jäggi, A. Michalowski, B. Neuenschwander, Review on experimental and theoretical investigations of ultra-short pulsed laser ablation of metals with burst pulses, Mater. (Basel) 14 (2021) 3331, https://doi.org/10.3390/ma14123331.
[12] B. Neuenschwander, B. Jaeggi, M. Schmid, G. Hennig, Surface structuring with ultra-short laser pulses: basics, limitations and needs for high throughput, Phys. Proced. 56 (2014) 1047–1058, https://doi.org/10.1016/j.phpro.2014.08.017.
[13] M. Seidel, L. Lang, C.R. Phillips, U. Keller, Ultrafast 550-W average-power thin-disk laser oscillator, Optica 11 (2024) 1368, https://doi.org/10.1364/OPTICA.529185.
[14] Z. Sun, M. Lenzner, W. Rudolph, Generic incubation law for laser damage and ablation thresholds, J. Appl. Phys. 117 (2015), https://doi.org/10.1063/1.4913282.
[15] C. Lutz, C. Esen, R. Hellmann, Ultrashort-pulsed laser processing with spatial and temporal beam shaping using a spatial light modulator and burst modes, IOP Conf.

Ser. Mater. Sci. Eng. 1135 (2021) 012026, https://doi.org/10.1088/1757-899X/1135/1/012026.
[16] A. Semerok, C. Dutouquet, Ultrashort double pulse laser ablation of metals, Thin Solid Film. 453–454 (2004) 501–505, https://doi.org/10.1016/j.tsf.2003.11.115.
[17] D.E. Roberts, A. du Plessis, L.R. Botha, Femtosecond laser ablation of silver foil with single and double pulses, Appl. Surf. Sci. 256 (2010) 1784–1792, https://doi.org/10.1016/j.apsusc.2009.10.004.
[18] J. Mildner, C. Sarpe, N. Götte, M. Wollenhaupt, T. Baumert, Emission signal enhancement of laser ablation of metals (aluminum and titanium) by time delayed femtosecond double pulses from femtoseconds to nanoseconds, Appl. Surf. Sci. 302 (2014) 291–298, https://doi.org/10.1016/j.apsusc.2013.09.137.
[19] M. Spellauge, J. Winter, S. Rapp, C. McDonnell, F. Sotier, M. Schmidt, H.P. Huber, Influence of stress confinement, particle shielding and re-deposition on the ultrashort pulse laser ablation of metals revealed by ultrafast time-resolved experiments, Appl. Surf. Sci. 545 (2021) 148930, https://doi.org/10.1016/j.apsusc.2021.148930.
[20] M.E. Povarnitsyn, T.E. Itina, K.V. Khishchenko, P.R. Levashov, Suppression of ablation in femtosecond double-pulse experiments, Phys. Rev. Lett. 103 (2009) 195002, https://doi.org/10.1103/PhysRevLett.103.195002.
[21] J. Winter, S. Rapp, M. Spellauge, C. Eulenkamp, M. Schmidt, H.P.H.P. Huber, Ultrafast pump-probe ellipsometry and microscopy reveal the surface dynamics of femtosecond laser ablation of aluminium and stainless steel, Appl. Surf. Sci. 511 (2020) 145514, https://doi.org/10.1016/j.apsusc.2020.145514.
[22] M.E. Povarnitsyn, T.E. Itina, P.R. Levashov, K.V. Khishchenko, Simulation of ultrashort double-pulse laser ablation, Appl. Surf. Sci. 257 (2011) 5168–5171, https://doi.org/10.1016/j.apsusc.2010.11.158.
[23] D.J. Förster, S. Faas, S. Gröninger, F. Bauer, A. Michalowski, R. Weber, T. Graf, Shielding effects and re-deposition of material during processing of metals with bursts of ultra-short laser pulses, Appl. Surf. Sci. 440 (2018) 926–931, https://doi.org/10.1016/j.apsusc.2018.01.297.
[24] A. Amouye Foumani, D.J. Förster, H. Ghorbanfekr, R. Weber, T. Graf, A.R. Niknam, Atomistic simulation of ultra-short pulsed laser ablation of metals with single and double pulses: an investigation of the re-deposition phenomenon, Appl. Surf. Sci. 537 (2021) 147775, https://doi.org/10.1016/j.apsusc.2020.147775.
[25] A. Žemaitis, P. Gečys, M. Barkauskas, G. Račiukaitis, M. Gedvilas, Highly-efficient laser ablation of copper by bursts of ultrashort tuneable (fs-ps) pulses, Sci. Rep. 9 (2019) 12280, https://doi.org/10.1038/s41598-019-48779-w.
[26] B. Bornschlegel, J. Finger, In-situ analysis of ultrashort pulsed laser ablation with pulse bursts, J. Laser Micro/Nanoeng.. 14 (2019) 88–94, https://doi.org/10.2961/jlmn.2019.01.0015.
[27] A. Žemaitis, M. Gaidys, P. Gečys, M. Barkauskas, M. Gedvilas, Femtosecond laser ablation by bibursts in the MHz and GHz pulse repetition rates, Opt. Express 29 (2021) 7641, https://doi.org/10.1364/OE.417883.
[28] A. Žemaitis, M. Gaidys, P. Gečys, M. Gedvilas, Bi-stability in femtosecond laser ablation by MHz bursts, Sci. Rep. 14 (2024) 5614, https://doi.org/10.1038/s41598-024-54928-7.
[29] B. Bornschlegel, M. Kratz, J. Finger, In situ analysis of ultrashort pulse burst ablation via transmission pump probe imaging, 17 (2022). https://doi.org/10.2961/jlmn.2022.01.2004.
[30] I. Zinovik, A. Povitsky, Dynamics of multiple plumes in laser ablation: modeling of the shielding effect, J. Appl. Phys. 100 (2006) 1–13, https://doi.org/10.1063/1.2217108.
[31] O.A. Ranjbar, Z. Lin, A.N. Volkov, Plume accumulation effect and interaction of plumes induced by irradiation of a copper target with a burst of nanosecond laser pulses near the ionization threshold, J. Appl. Phys. 127 (2020), https://doi.org/10.1063/5.0007786.
[32] M. Spellauge, D. Redka, A. Podhrazsky, K. Eckmann, C. Eulenkamp, O. Koepp, C. Doñate-Buendia, B. Gökce, S. Barcikowski, H.P. Huber, Mechanisms of laser ablation in liquids and their impact on the efficiency of nanoparticle generation, Laser Photon. Rev. (2025) 1–13, https://doi.org/10.1002/lpor.202501348.
[33] C. Momma, S. Nolte, B.N. Chichkov, F.v. Alvensleben, A. Tünnermann, Precise laser ablation with ultrashort pulses, Appl. Surf. Sci. 109–110 (1997) 15–19, https://doi.org/10.1016/S0169-4332(96)00613-7.
[34] N.A. Smirnov, S.I. Kudryashov, P.A. Danilov, A.A. Rudenko, B. Gakovic, D. Milovanović, A.A. Ionin, A.A. Nastulyavichus, S.F. Umanskaya, Microprocessing of a steel surface by single pulses of variable width, Laser Phys. Lett. 16 (2019) 056002, https://doi.org/10.1088/1612-202X/ab0c85.
[35] J. Hohlfeld, J.G. Müller, S.-S. Wellershoff, E. Matthias, Time-resolved thermoreflectivity of thin gold films and its dependence on film thickness, Appl. Phys. B Lasers Opt. 64 (1997) 387–390, https://doi.org/10.1007/s003400050189.
[36] I.A. Artyukov, D.A. Zayarniy, A.A. Ionin, S.I. Kudryashov, S.V. Makarov, P. N. Saltuganov, Relaxation phenomena in electronic and lattice subsystems on iron surface during its ablation by ultrashort laser pulses, JETP Lett. 99 (2014) 51–55, https://doi.org/10.1134/S0021364014010020.
[37] D. Bergström, J. Powell, A.F.H. Kaplan, The absorption of light by rough metal surfaces—A three-dimensional ray-tracing analysis, J. Appl. Phys. 103 (2008) 103515, https://doi.org/10.1063/1.2930808.
[38] T. Häfner, J. Heberle, M. Dobler, M. Schmidt, Influences on incubation in ps laser micromachining of steel alloys, J. Laser Appl. 28 (2016) 022605, https://doi.org/10.2351/1.4944445.
[39] J.M. Liu, Simple technique for measurements of pulsed gaussian-beam spot sizes, Opt. Lett. 7 (1982) 196, https://doi.org/10.1364/OL.7.000196.
[40] T. Pflug, M. Olbrich, J. Winter, J. Schille, U. Löschner, H. Huber, A. Horn, Fluence-dependent transient reflectance of stainless steel investigated by ultrafast imaging pump–Probe reflectometry, J. Phys. Chem. C. 125 (2021) 17363–17371, https://doi.org/10.1021/acs.jpcc.1c04205.
[41] C. Chen, M. Spellauge, D. Redka, R. Auer, C. Doñate-Buendia, S. Barcikowski, B. Gökce, H.P. Huber, L.V. Zhigilei, Time-resolved probing and modeling of optical signatures of ultrashort-pulse laser spallation and phase explosion in iron-nickel targets, Phys. Rev. B. 111 (2025) 174301, https://doi.org/10.1103/PhysRevB.111.174301.
[42] D. Von Der Linde, K. Sokolowski-Tinten, Physical mechanisms of short-pulse laser ablation, Appl. Surf. Sci. 154 (2000) 1–10, https://doi.org/10.1016/S0169-4332(99)00440-7.
[43] V.S. Gushchin, K.M. Shvarev, B.A. Baum, P.V. Gel'd, Influence of composition on optical properties and electronic characteristics of Fe-Ni alloys at high temperatures, Sov. Phys. J. 21 (1978) 882–885, https://doi.org/10.1007/BF00892042.
[44] M. Schmid, S. Zehnder, P. Schwaller, B. Neuenschwander, J. Zürcher, U. Hunziker, Measuring the complex refractive index of metals in the solid and liquid state and its influence on the laser machining, in: X. Xu, G. Hennig, Y. Nakata, S.W. Roth (Eds.), Laser Appl. Microelectron. Optoelectron. Manuf. XVIII, 2013 86071I, https://doi.org/10.1117/12.2003744.
[45] C.Y. Ho, R.W. Powell, P.E. Liley, Thermal conductivity of the elements, J. Phys. Chem. Ref. Data. 1 (1972) 32, https://doi.org/10.1063/1.3253100.
[46] R. Fang, A. Vorobyev, C. Guo, Direct visualization of the complete evolution of femtosecond laser-induced surface structural dynamics of metals, Light Sci. Appl. 6 (2016) e16256, https://doi.org/10.1038/lsa.2016.256.
[47] R.S. Graves, T.G. Kollie, D.L. McElroy, K.E. Gilchrist, The thermal conductivity of AISI 304L stainless steel, Int. J. Thermophys. 12 (1991) 409–415, https://doi.org/10.1007/BF00500761.
[48] A. Miloshevsky, S.S. Harilal, G. Miloshevsky, A. Hassanein, Dynamics of plasma expansion and shockwave formation in femtosecond laser-ablated aluminum plumes in argon gas at atmospheric pressures, Phys. Plasmas 21 (2014), https://doi.org/10.1063/1.4873701.
[49] B. Gonzalez-izquierdo, H. Sakurai, R. Yamada, K. Konishi, Plasma dynamics induced by single-pulse femtosecond laser ablation of dielectrics and metals, Laser. Manuf. Conf. (2021) 1440–1446.
[50] A.Y. Vorobyev, C. Guo, Enhanced absorptance of gold following multipulse femtosecond laser ablation, Phys. Rev. B. 72 (2005) 195422, https://doi.org/10.1103/PhysRevB.72.195422.
[51] F. Bauer, Residual heat in ultra-short pulsed laser ablation of metals, J. Laser Micro/Nanoeng. 10 (2015) 325–328, https://doi.org/10.2961/jlmn.2015.03.0016.
[52] D. Metzner, P. Lickschat, S. Weißmantel, Influence of heat accumulation during laser micromachining of CoCrMo alloy with ultrashort pulses in burst mode, Appl. Phys. A 126 (2020) 84, https://doi.org/10.1007/s00339-019-3203-7.
[53] B. Neuenschwander, T. Kramer, B. Lauer, B. Jaeggi, Burst mode with ps- and fs-pulses: influence on the removal rate, surface quality, and heat accumulation, in: S. Roth, Y. Nakata, B. Neuenschwander, X. Xu (Eds.), Proc. SPIE - Int. Soc. Opt. Eng., 2015 93500U, https://doi.org/10.1117/12.2076455.